Functional Nanostructured Materials (including low-D carbon)

Lignin particles for multifunctional membranes, anti-oxidative microfiltration, patterning and 3D structuring

Oriol Cusola, Orlando J. Rojas, and M. Blanca Roncero

ACS Appl. Mater. Interfaces, **Just Accepted Manuscript** • DOI: 10.1021/acsami.9b16931 • Publication Date (Web): 08 Nov 2019

Lignin particles for multifunctional membranes, anti-oxidative microfiltration, patterning and 3D structuring

Oriol Cusola[1,2*], Orlando J. Rojas[2,3], M. Blanca Roncero[1]

[1]CELBIOTECH Research Group, Escola Superior d'Enginyeries Industrial, Aeroespacial i Audiovisual de Terrassa, Spain.

[2]Department of Bioproducts and Biosystems, School of Chemical Engineering, Aalto University, FI-00076 Aalto, Finland.

[3]Department of Chemical and Biological Engineering, University of British Columbia, Canada.

**Corresponding author e-mail address: oriol.cusola@upc.edu (Oriol Cusola)*

ABSTRACT

We introduce a new type of particle-based membrane based on the combination of lignin colloids (LP) and cellulose nanofibrils (CNF), the latter of which are introduced in small volume fractions to act as networking and adhesive agent. The synergies that are inherent to lignin and cellulose in plants are re-engineered to render materials with low surface energy (contact angle measurements) and that can be rendered water resistant with the aid of wet-strength agents (WSA). Importantly, they are most suitable for anti-oxidative separation ($ABTS^{\bullet+}$ radical inhibition): membranes with uniform porous structures (air permeability and capillary flow porosimetry) allow effluent oxidation at 95 mL/cm^2, demonstrating, for the first time, the use of unmodified lignin particles in flexible membranes for active microfiltration. Moreover, the membranes are found to be non-fouling (protein adhesion and activity rate). The inherent properties of lignin, including UV radiation blocking capacity (UV transmittance analysis) and reduced surface energy are further exploited in the development of tailorable and self-standing architectures that are almost entirely comprised of non-bonding LP (solids content as high as 92 w/w%). Despite such composition, the materials develop high toughness (oscillatory dynamic mechanical analysis), owing to the addition of minor amounts of CNF. Multifunctional materials based on thin films (casting), 3D structures (molding) and patterned geometries (extrusion deposition) are developed as a demonstration of the potential use of lignin particles as precursor of new material generation. Remarkably, our observations hold for spherical LPs since a much poorer performance was observed after using amorphous powder, indicating the role of size and shape in related applications.

KEYWORDS: Lignin particles, antioxidant, membrane microfiltration, cellulose nanofibres, 3D structures

1. Introduction

Synthetic materials have led to major leaps in our quest to solve many of the needs of our industrialized society. However, recent efforts have been made to adopt new, biobased materials and composites as alternatives to those based on fossil-based resources. As part of these efforts and within the future bioeconomy, plant-based biopolymers are being investigated. They include lignin, a randomly cross-linked polymer comprising phenylpropane units bonded with diverse inter-unit linkages. Following natural evolution in plant biogenesis, lignin has evolved to contribute with multiple roles, including those related to the structural integrity and functional properties. The latter include protection against radiation and fire, antioxidant, antifungal, UV blocking as well as antimicrobial and antibacterial activities [1–3]. Fluid transport through the vasculature system is also regulated by lignin [4]. It is thus expected that lignin can be utilized in the synthesis of functional materials, exploiting other inherent properties such as its high thermal degradation temperature and, depending on the source and processing conditions, its surface and wetting properties, rheological and viscoelastic behaviors. The development of lignin films compatible with a wide variety of commodity chemicals is only an example of the many sues that can be anticipated [5], especially in the context of the so-called lignin biorefineries [6–9], where aromatic units are depolymerized to isolate the monomers and upgraded towards targeted chemicals. They include binding agents, bio-dispersants and emulsifying agents, as well as a precursor for the synthesis of thermoplastics [10–12].

Recent efforts have incorporated lignin in complex materials where other polymers are used as structural matrices [13]. Even when present in small amounts, the intrinsic properties of lignin makes a major contribution to those composites. Agar films [14], poly(butylene succinate) films [15], soy protein isolate films [16], or nanocellulose-based films [17,18], are but a few examples of such composites. However, and most interestingly, in such efforts lignin use has been limited to addition levels amounting to less than 10 % of the total dry weight. One of the reasons to incorporate lignin in such small amounts is to avoid the typical rigidity and brittleness that would otherwise result when lignin is the dominant component. This mainly caused by its natural condensed structure and strong intermolecular hydrogen bonding, which restrict thermal mobility [19]. An exception to these observations is the nearly all-lignin films that were introduced recently, [20] in the form of supported layers deposited on silica or quartz surfaces, for uses in biosensing[21–24]. In addition, 3D-printed lignin structures have been reported *via* fused deposition. Here lignin was introduced in the formulation of thermoplastic filaments at levels reaching values as high as 40 wt % with ABS [25,26], 30 wt % with PP [27], and 20 wt % with PLA [28,29]. Finally, lignin-based foams have been prepared with lignin content of up to 55 wt % [30,31]. However, no commercially available foams exist using technical lignins as the main component [32]. Overall, the manufacture of all-lignin films and 3D materials remains intractable. To address this challenge, we exploit the structuring ability of lignin when used as a spherical micro/nano-particulate, opening a new perspective for its utilization. This builds upon previous efforts to incorporate lignin in polymer blends [33–35] and our

previous work, which demonstrated particulate films by self-assembly and stratification of lignin particles (LPs) upon drying [20]. In such efforts, however, two major drawbacks remain: the non-cohesive nature of the systems and the lack of water resistance. Moreover, capillary stresses generated upon drying is a challenge that prevents film consolidation. Hence, we propose cellulose nanofibrils (CNF) as a possibility to overcome these challenges, even if added as a minor component. A recent report, for instance, combined lignin particles with CNF, using equivalent amounts of each component[36].

Herein, we introduce a new methodology to synthesize membranes containing up to 92% lignin particles using CNF to enable adhesion and structuring and to allow handleability, flexibility and water resistance. The functional properties of lignin are further exploited in the development of micro- and nanofiltration membranes with antioxidant capability. They are expected to be most suitable for hemodialysis (for the reduction of reactive oxygen species in blood) [37], in fuel cells (to avoid hydrogen peroxide and hydroxyl radicals deterioration)[38], and in water treatment [39,40]. The efforts are expanded to the design of 3D materials via molding and patterned deposition, taking advantage of the rheological properties of LPs-CNF suspensions that greatly facilitate extrusion.

2. Materials and Methods

2.1. Materials

Kraft lignin (Indulin AT, Mead Westvaco, USA) was used as received to produce lignin particles via an aerosol-flow reactor, as reported previously [41]. Prior dissolution in dimethylformamide, the lignin particles were synthesized using a collison-type jet atomizer with nitrogen gas as carrier. The generated droplets were suspended at a nitrogen gas flow rate of 3 L/min and carried to a heated laminar flow stainless steel tube with an inner diameter and length of 30 and 80 mm, respectively, and kept at 153 °C. During flow-through, the droplets were dried into solid particles, which were subsequently cooled and diluted at the reactor downstream with a turbulent air flow volume of 30 L/min before collection. Cellulose nanofibers (CNF) were obtained from the Process Development Center at University of Maine at 3.0 w% hydrogel, with a specific surface of 31-33 m^2/g (BET), a density of 1.0 g/cm^3, and a nominal size of 50 nm in length and up to several hundred microns in length. Polyamidoamine-epichlorohydrin resin (Eka WS 505) was supplied by Akzo Nobel Chemicals®, El Prat de Llobregat, Barcelona, Spain (20 ± 0.5 (w/w) solid content, 1.06 g/cm^3 at 20°C, and 70–130 mPa·s Brookfield viscosity).

2.2. Preparation of membranes, patterned and 3D structures

Self-standing membranes were prepared by dispersing dry LPs (8%) in an aqueous CNF (0.4% w/v) suspension followed by casting onto polypropylene 5 (PP5). Prior to casting, the substrate was rinsed with ethanol and acetone, and the casting area was delimited

using adhesive laminate. Finally, the membranes were dried under ambient conditions. The areal mass of the resulting membranes was 35±5% g/m^2 with a 40-50 µm in thickness. To prepare water-resistant LPs membranes, 0.2% (w/v) polyamidoamine-epichlorohydrin resin was added as wet strength agent (WSA) with subsequent curing at 105^{o}C for 20 minutes. Pure CNF membranes and LPs-CNF membranes were prepared as control. UV transmittance analysis was carried out by casting the exact amounts of a 0.4% CNF suspension (or LPs-CNF, for membranes with varying LPs content) onto a 70x50 mm polypropylene cuvette to obtain 35 g/m^2 membranes.

For 3D molding, a photopolymer resin was used to build a mold with the desired shape, where the LPs-CNF suspension was casted. Suspension aliquots were introduced after each drying cycle (30 min.) until the desired thickness of the structure was achieved. Finally, it was de-molded and cured, as explained previously. For patterning, an automatic syringe pump was used. The LPs-CNF suspension was introduced into a syringe and extruded through a 0.91 mm Ø needle at a constant speed. The desired shape was achieved by the lateral movement of the deposition plane along the x and y axis.

2.3. SEM analysis

Scanning electron microscopy (SEM) images of the LPs-CNF membranes cross sections and surface were obtained using a Zeiss Sigma VP, Germany, with an acceleration voltage of 2 kV. Before imaging, the samples were sputtered with a 3 nm platinum layer.

2.4. Antioxidant capacity measurement

The antioxidant capacity of membranes was measured by using a variation of the method used by Serpen et. al.,[42] by quantification of the ABTS$^{\bullet+}$ radical inhibition and as previously reported [43,44]. First, the ABTS radical cation was generated by reacting potassium persulfate with the ABTS salt. Then, 10 mg of membrane were introduced into microcentrifuge tubes with a variable volume of ABTS$^{\bullet+}$ solution, depending on the inhibition capacity of the sample. Next, the tubes were agitated using a vortex mixer for 2 min to facilitate surface reaction, centrifuged (4 min 6000 rpm), and allowed to stand for 30 min. Following, absorbance measures were performed by taking 1 mL of the supernatant and placing it into a methacrylate cuvette. The absorbance value of each sample at 752 nm was monitored every minute up to 6 min, or until stabilization [44] by UV–Vis spectrophotometry, using a Thermo Scientific Evolution 600 instrument. The reduction in ABTS$^{\bullet+}$ concentration, induced by a certain amount of antioxidant, was related to that of Trolox (a standard reference antioxidant compound), via a pre-made calibration curve. Finally, the antioxidant capacity expressed as Trolox concentration per mg of membrane was calculated as follows:

$$AC = \frac{C_T}{m_f} \cdot \frac{V_{ABTS^{\bullet+}}}{990} \quad [1]$$

where *AC* is the antioxidant capacity (mmol of Trolox / mg of membrane), C_T is the Trolox concentration, mmol, m_f is the mass of membrane, mg, $V_{ABTS^{\bullet+}}$ is the volume of

ABTS$^{\bullet+}$ used in the determination of *AC*, and 990 is a factor accounting with the amount of ABTS$^{\bullet+}$ used in the Trolox calibration curve.

To test the membranes as antioxidant filters, the membranes were cut into circular shapes (Ø=2.5 cm), and introduced into a Sartorius™ Stedim Stainless-steel Syringe Filter Holder. Then, the ABTS radical was generated at a given concentration ($c_0^{\bullet+}$) and the ABTS$^{\bullet+}$ solution was filtered using constant pressure filtration with a *ΔP* of 10k Pa. Several aliquots of the filtered ABTS$^{\bullet+}$ solution were withdrawn at different volume intervals, and the concentration of the remaining radical ($c_f^{\bullet+}$) was measured using UV-Vis.

2.5. Pore size distribution and Air and water permeability

The pore size was determined using a Quantachrome 3Gzh instrument by capillary flow porosimetry. The wetting liquid (commercial Porofil®) was used to fill the pores of the sample. A non-reacting gas (air) was then used to displace a liquid from the pores. Provided that the work done by the gas is equal to the surface free energy required for the replacement of the low free energy liquid, the capillary equilibrium can be expressed as:

$$P \cdot r = 2\gamma cos\theta \quad [2]$$

where *r* is the radius of the capillary, *P* is the capillary pressure, γ is the surface tension of the liquid, and θ is the contact angle between the liquid and the capillary wall. Porosity and permeability were measured by cutting circular membranes (Ø=2.5 cm). For pore number measurements, the membranes were first immersed in Porofil®, and introduced in the sample holder. The pressure was scanned over a range of 0.1 to 1 bar and 0.1 to 10 bar in the case of Whatman® 1 paper, and LPs membranes respectively. The instrument measures the air flow through the wet sample and detects the bubble point pressure (the pressure at which gas flow begins through wet sample), to compute the largest pore diameter. The pressure is transformed to pore size using **equation 2**. The pore number distribution, was determined using the Hagen-Poiseuille Equation:

$$Q = \frac{N\pi r^4 \Delta P}{8\eta l} \quad [3]$$

where Q is the flow rate of air, η the air viscosity, *ΔP* the differential pressure through a number of cylindrical pores, *N* is the number of pores, *r* the radius of pores, and *l* their length. The pore length is defined as the sample thickness x tortuosity. Tortuosity is assumed 1 for cylindrical pores. The smallest pore diameter is determined as the pressure at which the dry and the wet curves meet. Finally, in order to find the mean flow pore diameter, the half-dry curve is first computed to yield half of the flow rate through dry curve at a differential pressure. The pressure at which the wet curve intersects the half-dry curve is used to compute the mean flow pore diameter. The mean flow pore diameter is such that half of the flow is evacuated through pores larger than the mean pore diameter.

The air permeability was tested over a pressure range of 1 to 30 kPa on dry samples. To measure water permeability, a special setup consisting in a metallic liquid tank was used. The pressure was scanned in all specimens over a range of 1 to 100 kPa.

2.6. UV blocking properties

The UV blocking properties were tested using a Labsphere UV-1000P Ultraviolet Transmittance Analyzer over a wave range of 290 to 400 nm (UVA and UVB) with a wavelength accuracy of 2 nm and a transmittance accuracy of ± 0.5%T. The equipment measured the diffuse transmittance of the sample using a dual diode array spectrometer with a Xenon flashlamp, optimized for UV emission, and an integrating sphere. Multiple scans were averaged and the mean value was reported. For the transmittance measurements several LPs-CNF membranes with a varying content on LPs were produced as indicated previously. The membranes were directly placed into the measuring holder and measured without further conditioning.

2.7. Dynamic mechanical analysis

Dynamic mechanical analysis (DMA) was performed on membranes with increased CNF loading (4 to 20%) using a DMAQ800 unit (TA Instruments, New Castle, DE, USA) operating under tensile testing mode, and using a preload of 0.1 N. The gauge length was adjusted to 14 mm. The measurements were performed at a constant temperature (30°C) and a sinusoidal (dynamic) tensile load (1 kHz) was applied to produce a dynamic strain with constant amplitude of 0.05%.

2.8. Contact angle measurements

Water contact angle (WCA) was measured using an OCA15 contact angle goniophotometer (Dataphysics). First, the membranes were cut into 40x5mm stripes and mounted onto a sample holder. Then, a 4 µL droplet was placed on the surface of the sample and the contact angle was monitored over time by ellipse fitting. The surface free energy (SFE) was evaluated using the Owens, Wendt, Rabel and Kalble (OWRK) method. Briefly, several drops of deionized water, ethylene glycol and diiodomethane were applied to the surface of the samples and the corresponding contact angles were measured. At least five droplets of each liquid were dispensed in different regions. The total surface free energy was computed as the sum of the polar and disperse contributions. The interfacial energy was calculated according to OWRK from the contributions of the liquid and the solid by forming the geometric mean:

$$\sigma_l(1 + cos\theta) = 2\sqrt{\sigma_l^d \sigma_s^d} + 2\sqrt{\sigma_l^p \sigma_s^p} \quad [4]$$

here, θ is the contact angle, σ_l the surface tension of the liquid, σ_l^d and σ_l^p represent the disperse and polar parts of the liquid, while σ_s^d and σ_s^p stand for the respective contributions of the solid. This gives an equation of a straight line which allows calculation of σ_s^p from the slope of the fitted line and σ_s^d from the intersection with the vertical axis.

2.9. Protein adhesion assessment

Protein adhesion was determined by introducing the membranes in a lysozyme enzyme solution (1.5 mg/mL; 58 KU/mL ±300) under gentle agitation at constant temperature (25°C), and measuring the remaining activity at different time intervals. The activity was measured by monitoring the lysis rate of a 0.01% (w/v) suspension of *Micrococcus lysodeikticus* cells. After mixing the enzyme (0.1 mL) with the microorganism (2.5 mL), the decrease in absorbance at 450 nm was recorded for 5 minutes using a suitably thermostatic spectrophotometer to obtain the maximum linear rate (ΔA450/minute). Then, the enzyme activity was obtained using the following equation:

$$Units/ml\ enzyme = \frac{\left({}^{\Delta A_{450}}/_{\min Test} - {}^{\Delta A_{450}}/_{\min Blank}\right) \cdot (df)}{(0.001) \cdot (0.1)} \quad [5]$$

where d_f is dilution factor, 0.001 is the ΔA_{450} as per the unit definition, and 0.1 is the volume (in milliliters) of enzyme solution.

3. Results and Discussion

3.1. Lignin-based particulate membranes

As reported in our previous work, layers of structured lignin can be easily produced using evaporation-induced self-assembly [20]. However, they require solid supports given the lack of cohesion of the structure. Some solutions to this challenge have been found by exploiting physicochemical interactions with cationic polyelectrolytes, such as polyDADMAC; coordination with complexes using natural polyphenols and Fe(III) ions [45,46]; activation with laccase enzymes; combination with gelatin as a biodegradable adhesive to bind and cross-link the particles [47]; and amidation using proteins and DMTMM [48]. However, these methods have not been fully effective given the limited mechanical properties and brittleness observed for these systems. In the search for linking agents that provide good coupling efficiency and result in flexible films, cellulose nanofibers (CNF) can be considered as suitable candidates. In this regard, recent work has revealed the ability of CNF to promote adhesion in biogenic silica particles, allowing superstructures with well-controlled morphologies [49].

Here, self-standing and lignin-rich membranes were produced by incorporating small amounts of CNF, which not only brings the benefits of being natural, biodegradable, and renewable but, above all, displays a high affinity to lignin in terms of hydrogen-bonding interactions and has a large aspect ratio, allowing entanglement within the membrane's structure. In fact, after CNF incorporation, even in small amounts (<10% of total dry mass), the membranes were found to be crack-free, homogeneous and, interestingly, were easily peeled off from the polyolefin support, producing self-standing and robust membranes (**Figure 1a**). The high affinity between the two components, the cohesion and the flexibility furnished by CNF allows the development of self-supporting membranes. SEM images of their cross sections reveal a porous

structure in which the CNF is embedded within the LPs (**Figure 1b**). The lowest CNF loading to ensure self-standing and cohesive membranes was found by systematic variations in the composition using CNF suspensions at concentrations in the range 0.05-1% (w/v). Upon drying, the membranes with the lowest concentrations on CNF in the suspension (i.e. 0.05 - 0.4%) were nonhomogeneous, and incorporated aggregates and defects. **Figure 1c** shows a ternary composition diagram that includes the inventory of LNPs, CNF and wet strength agent, WSA. It displays a region marked in pink that correspond to systems with good observed cohesion. The one in green color indicates the composition that develops poor cohesion. We aimed to develop systems in the upper vertex of the diagram, in the composition zone where the LPs are the main structural component. This is in contrast to the systems produced with compositions in the bottom corner of the ternary diagram, which corresponds to LPs-reinforced CNF membranes (CNF as major structural component). The 0.4% CNF suspension was chosen as standard to produce the membranes in the subsequent tests. This amount of CNF represented only the 8% of the total dry weight but still ensuring membranes that are self-standing.

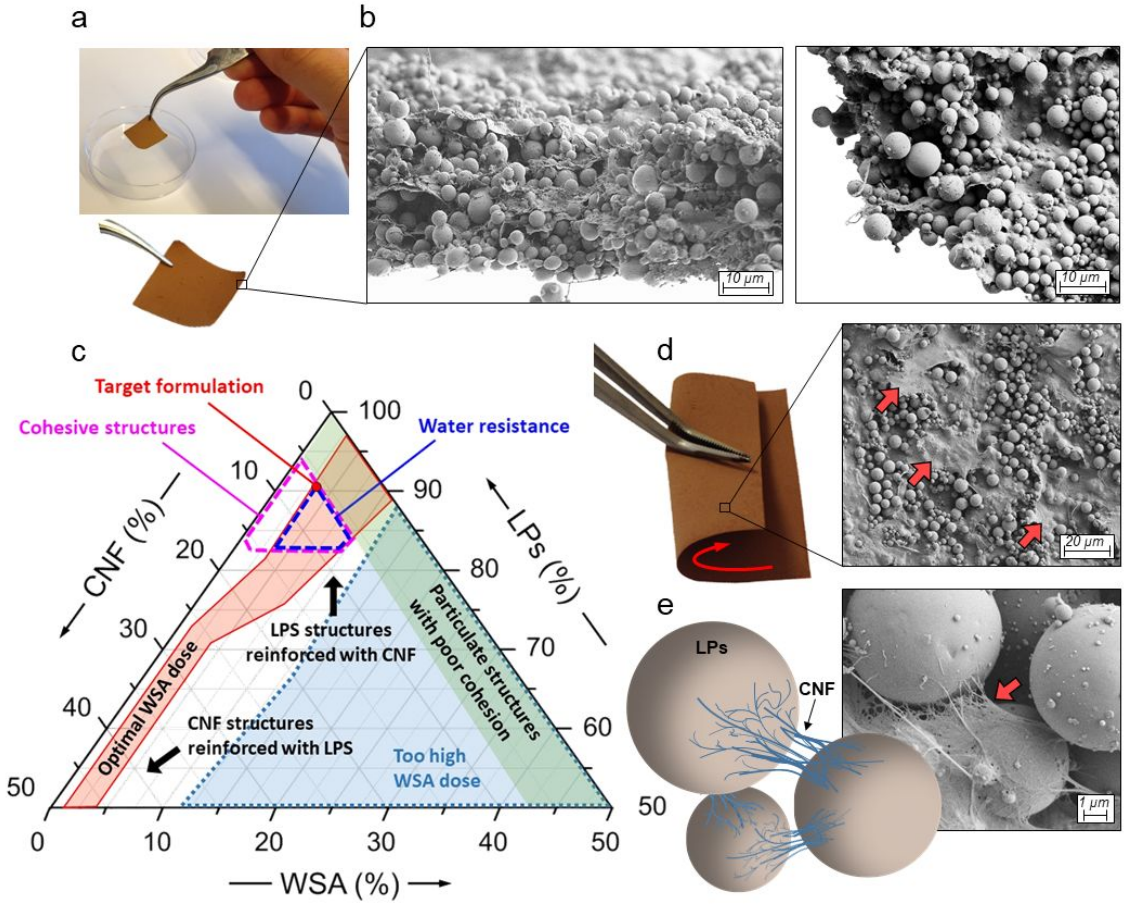

Figure 1. Self-standing LPs-CNF membranes (shown in (a) is the case of systems with 8% wt CNF). SEM cross-sections of the membrane in (a) are shown in (b). Ternary phase diagram indicating the composition (LP, CNF, WSA) that leads to membranes with good cohesion and water-strength, including the optimal conditions for maximizing LP loading while allowing for water resistance (c). The flexibility and folding

ability of LP-based membranes is illustrated with a photo in (d), along with a SEM image of the surface morphology where CNF formed continuous film regions (d, red arrows). Schematic diagram and SEM image showing the role of the CNF bridging the particles together within the particulate structure (e).

The membranes tested are lignin-rich yet very flexible, as shown in **Figure 1d**. Moreover, **Figures 1b and 1d**, indicate the regions in which CNF tended to form continuous membranes, by virtue of its widely known film-forming ability, a tendency that was disrupted by the presence of LPs. It is reasonable to assume that CNF act as particle-linker through –OH interactions between cellulose and lignin, although it is difficult to draw conclusive evidence on the hydrogen-bond interaction between CNF and LPs, at least by FTIR (See **Figure S1** in the Supporting Information file). Thus, in the membranes, the dominant contribution of lignin mask the fingerprint peaks of cellulose. The high flexibility of the obtained membranes benefited from CNF's ability to act as inter-particle bridges (**Figure 1e**) and given its contribution to the flexibility, even if added in small amounts.

The rheology of the aqueous suspensions (LP, CNF and LPs-CNF mixtures) was hypothesized to allow for the optimal CNF-to-LPs ratio that promotes effective insertion of CNF within the LPs matrix, as depicted in **Figure S2a** (see Supporting Information file). A CNF loading of 8% is found to preserve flowability and to enable membrane formation. The LP and CNF aqueous suspensions are shear-thinning (**Figure S2b**), due to the particle ordering under shear with the viscosity of the LPs-CNF mixture being slightly higher than that of the CNF alone (**Figure S2c**).

3.2. Water-resistant membranes

The water strength of the LPs-CNF membranes was tested by immersion in water under agitation. As shown in **Figure 2** (right image, without WSA), the membranes easily disintegrate in water preventing their use in related applications, including heterogeneous catalysis and filtration (see video supplied as Supporting Information). In order to develop self-standing and water-resistant LP-based membranes, a wet strength agent (WSA) was added during the membranes preparation. Several membranes with given amounts of WSA, between 0.5 and 10 mg/mL, were produced and tested for their water strength. The optimal WSA loading in the LPs-CNF membranes is shown in red in **Figure 1c**. The optimal composition for favorable cohesion corresponds to a WSA loading of 2 mg/mL, in which a significant increase in water resistance is produced, **Figure 2** (right image, with WSA). Such membranes preserve their flexibility and mechanical properties. Even after successive immersion-drying cycles, the membranes maintain a strong cohesion upon immersion in the aqueous medium. WSA addition in excess to 10%, would produce rigid structures saturated in WSA.

We observed a minimal LPs leaching from the membranes, about 0.5% of the total mass of the film. The leaching study is included as Supporting Information (**Figures S3 and S4**). We speculate that this small leaching mainly occur once the film was immersed in water, due to the non-bound lignin particles. This means that with an initial rinsing, the leaching can be reduced even below this figure.

As a result of these water resistance studies, a LP-CNF-WSA membrane was selected to be used for further work in applications requiring water-resistant membranes, (90% LP, 7% CNF, and 3% wt WSA, **Figure 1c**). Contrarily, in applications or measurements not requiring water resistance, the composition of the membranes was (92% LP, and 8% wt CNF).

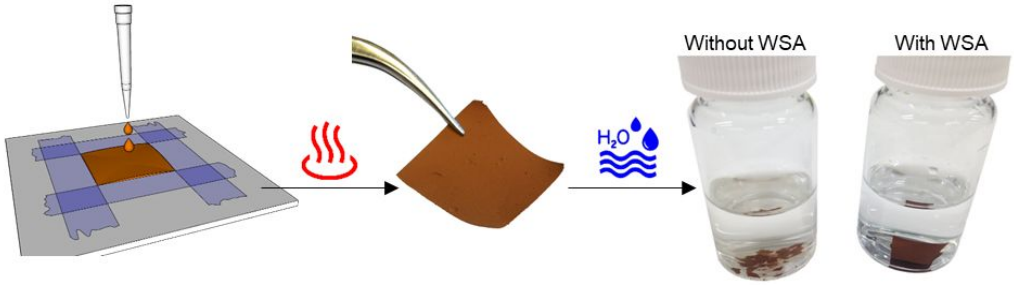

Figure 2. Membrane casting on a flat support, photo of the obtained membrane, and illustration of a test for water resistance after treatment with WSA.

3.3. LP-based membranes, porosity and permeability

The LPs-CNF-WSA membranes show a porous structure that together with their wet strength indicates potential use as filtration media. The pore size of LP-based membranes was measured and compared with that of Whatman® 1 filter paper, which is of common use. The pore structure of membranes prepared with single component CNF was not possible to assess with the applied experimental approach; considering the high-density structure and the very small pore size that required very high pressures (lower limit 0.2 µm). Several works have reported on the pore structure of CNF films. Porosity can be measured, for example, by weight difference prior and after absorption of electrolyte. Porosity in CNF films typically ranges between 50-70%, depending on the film-formation technique used [50,51], with pore diameters in the sub-micrometric region, typically between 5-200 nm [52,53]. The tortuosity (τ) and form (c) factors were determined in an effort to describe a system that is more complex than that described by the cylinder pore model. The values for Whatman® 1 paper were taken as $\tau = 2$ [54] and $c = 0.75$ [55,56]; those for LP-based membranes were $\tau = 1.1$ [57–59] and $c = 0.9$ [56,60]. The contact angle of the testing liquid against the samples was measured (26° and 23° for Whatman® 1 and LP-based membranes, respectively). As shown in **Figure 3a**, the pore size distribution of the filter paper (blue line) show three well-defined populations (average pore diameter of 3, 3.5 and 4.2 µm). Less-significant small populations also appear between 2-2.7 µm. The inset in **Figure 3a** shows the maximum, minimum, and mean pore size values. The obtained mean pore value (4.5

µm) is taken as a reference for comparison, but it is important to note that 90% of the pores are below this size, as indicated by the cumulative profile. A Gaussian pore size distribution was obtained for the LP-based membranes, as shown in **Figure 3b**. In this case, the mean pore value (0.71 µm) accounts for the 50% of the cumulative data, as is typical of normal distributions.

The results clearly indicate that compared to filter paper, the LP-based membranes are smaller in pore size. However, their structure is more homogeneous, as shown by the normal size distribution. Given their smaller pore sizes, a lower fluid permeability was expected. Indeed, the permeability is significantly higher for the filter paper, more evident in the case of air transport, **Figures 3c and 3d,** respectively. For pressures > 80 kPa, the water permeability of LP-based membranes surpasses that of the filter paper, **Figure 3d**. Remarkably, the LP-based membranes, containing only 8% of networking CNF and 92% of particles, resist the high pressures imposed during transport experiments in the filtration unit.

The measured porosity of the membranes reveal a very homogeneous pore structure within a narrow range of sizes between 0.6 and 0.76 µm. Thus, the LP-based membranes constitute an interesting media for filtration using crossflow configuration. For example, these membranes are proposed for micro- and ultrafiltration operations, where they might retain pigments, bacteria, dyes or viruses, among other colloids. For industrial implementation the membranes may need to withstand pressures in the range from 0.2 to 1 MPa. Therefore, the LP-based membranes would act as selective layer in combination with another porous support that provides mechanical strength, as in a multilayer composite structure [61].

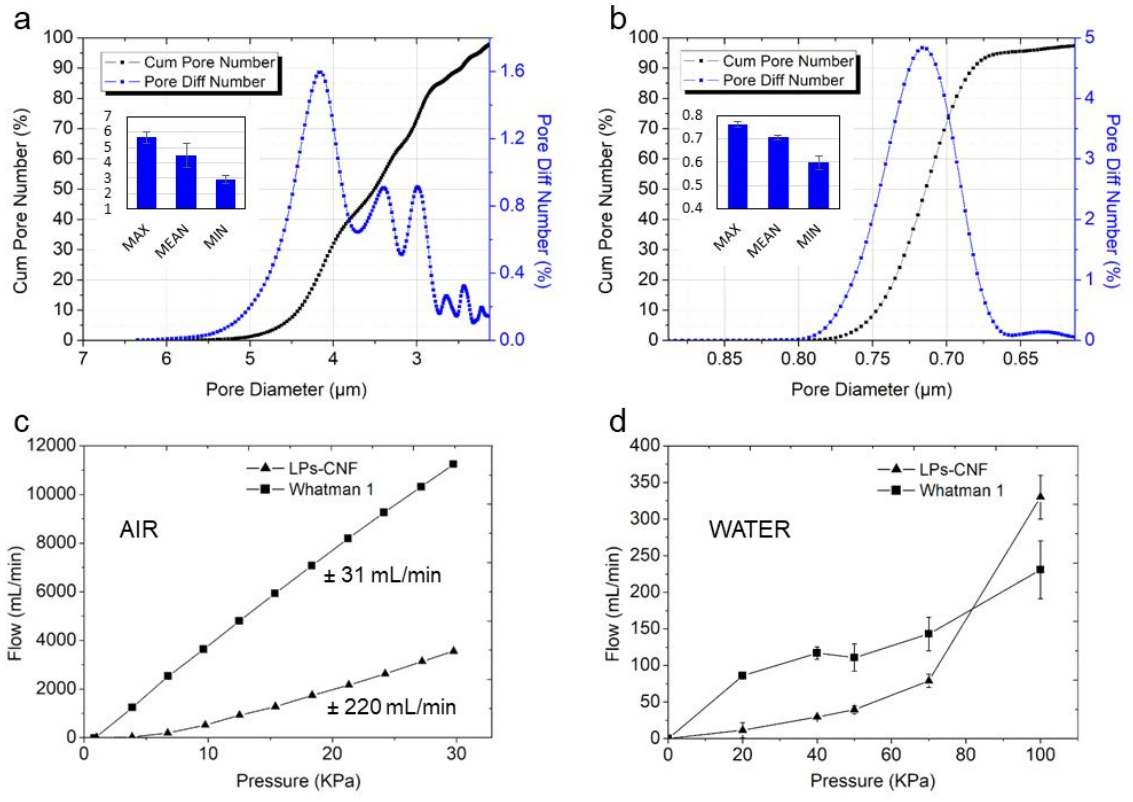

Figure 3. Pore size distribution, number and cumulative for Whatman® 1 filter paper and LP-based membranes (a and b, respectively). Insets in a and b indicate the maximum, mean and minimum pore sizes in µm. Air (c) and water (d) permeability of Whatman® 1 paper and LP-based membranes.

3.4. Antioxidant microfiltration

The antioxidant capacity, defined here as the ability to inhibit the oxidation rate of a free radical, is a known intrinsic property of lignin. Hence, the LP-based membranes were tested for their antioxidant capacity (**equation 1**) and compared to that of single-component CNF membranes. The antioxidant capacity of LP-based and single component CNF membranes correspond to 824 ± 25 µmol trolox/mg and 0.9 ± 0.08 µmol trolox/mg, respectively. Thus, the antioxidant capacity of the LP-based membranes is 1000-fold higher than that of those of CNF. Given the water strength, water permeability, and antioxidant capacity of the LP-based membranes, they were tested for active filtration under constant pressure (**Figure 4a**). The results for pore size and the water permeability make the membranes to fall in the microfiltration category.

The high antioxidant capacity of the membranes can be easily identified by color change corresponding to $ABTS^{\bullet+}$ radical shifting from blueish to clear color after filtration, **Figure 4b**. As shown, Whatman® 1 paper did not produce any color change to the radical solution whereas the LP-based membrane completely decolorized the radical by reduction via electron donation. **Figure 4c** shows the UV-Vis spectra of the initial $ABTS^{\bullet+}$ radical solution and that of the different filtered aliquots. As shown, there is a clear reduction in absorbance upon filtration, promoted by the antioxidant action of the membrane. It can be observed that in the first mL of the filtrate, the radical is completely inhibited; after filtration of a certain volume, the absorbance starts to gradually increase, indicating a limiting inhibition level, reaching a stabilizing value of about the 50% of the initial $ABTS^{\bullet+}$ absorbance. **Figure 4d** shows the evolution of the $ABTS^{\bullet+}$ absorbance peak at 731 nm vs. the filtered volume. As shown, the absorbance increased quickly in the first 20 mL (up to 50% abs.) but then the increase proceeded in a gradual manner, reaching a plateau at an inhibition corresponding to 50% of the initial $ABTS^{\bullet+}$ absorbance, following a first-order kinetic. This is indicative of the strong ability of the membranes to act as antioxidant filters. The antioxidant ability of the lignin particles in the membranes comes from their surface-active groups. As the fluid passes through the material, the antioxidant active groups deprotonate, giving electrons to the $ABTS^{\bullet+}$, inhibiting the radical. In the first stages of filtration, the number of such active groups is very high with a clear inhibition behavior, and decreases as the filtration takes place. Therefore, two stages can be identified for the inhibition performance. Integrating the first order expression between the beginning of the stabilization and 100% absorbance, the following expression is obtained:

$$ln\left[\frac{A}{A_0}\right] = kV \quad [4]$$

where, k is the first-order rate constant, A and A_0 are the ABTS$^{\bullet+}$ absorbance values at filtered volumes of V and V_0, respectively. With this, the theoretical maximum filtered volume before complete depletion of the inhibitory groups on the surface of the particles can be obtained. Using the kinetic constant, 0.0023, and the theoretical maximum volume, 298 mL, gives a maximum volume per unit area of 95 mL/cm^2. This filtration capacity is specific for each setup used. It is expected that for different filtration pressures, the filtration speed and the concentration of the ABTS$^{\bullet+}$ play an important role in the inhibition rate.

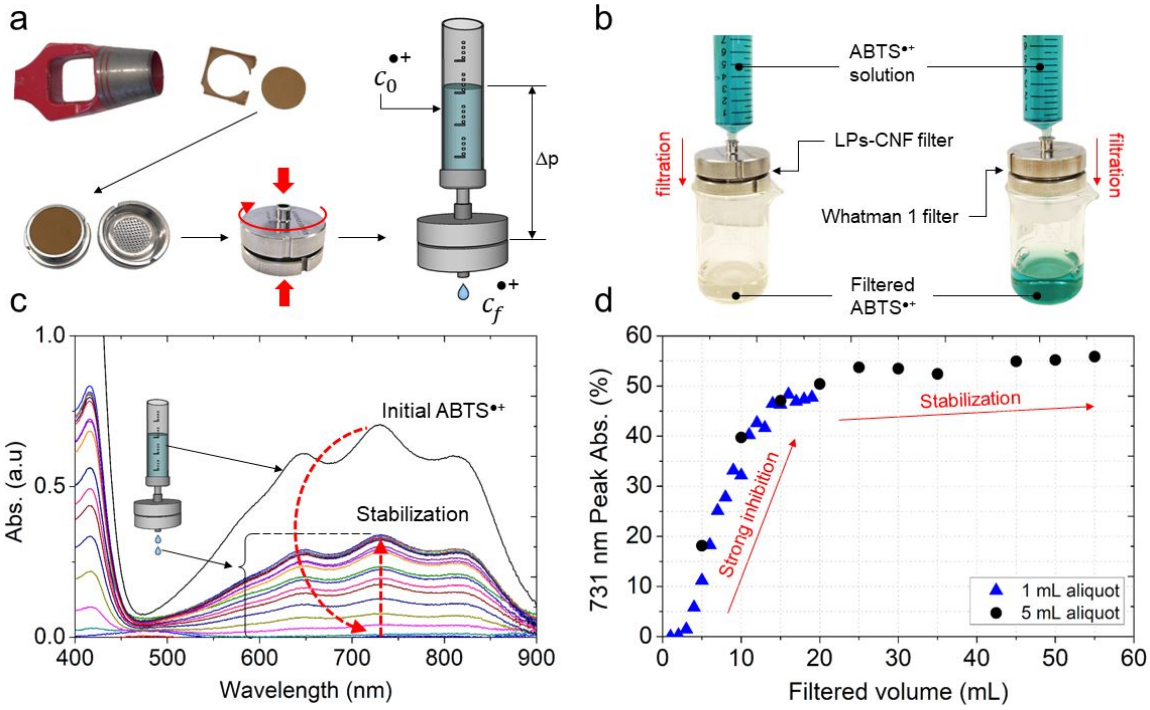

Figure 4. Assembly of LP-based membranes and mounting on a Sartorius™ Stedim stainless-steel Syringe Filter Holder for constant pressure filtration of a cationic radical (a). Filtration of ABTS$^{\bullet+}$radical solution using Whatman® 1 filter paper (right) and LP-based membranes (left); the remarkable decolorization of the blueish ABTS$^{\bullet+}$ radical after passage through the LP-based membrane is clearly seen (b). UV-Vis spectra of the initial ABTS$^{\bullet+}$ radical and evolution after passage through the LP-based membrane; a clear decrease and further stabilization is depicted (c). Evolution of the ABTS$^{\bullet+}$ radical 731 nm peak after filtration through the ABTS$^{\bullet+}$ radical (as % of the initial absorbance) taken after filtration of 1 mL aliquots (▲) and 5 mL aliquots (●) (d).

3.5. UV blocking, surface energy, mechanical and fouling resistance of LP-based membranes

LP-based membranes synthesized with increasing LP loading were investigated in terms of their capacity to block light radiation. As shown in **Figure 5a,** the pure CNF

membrane present a UV transmittance between 50-70%, depending on the UV region considered (UVB or UVA). The introduction of only 5% LP in the membranes produce a significant decrease of transmittance, down to 7-15%. With the introduction of 10% LP, the transmittance falls to 2-4%. LP loadings > 15% produce a full UV blocking effect. The evolution of the transmittance as a function of the LP content is better observed in the inset of **Figure 5a**. As shown, no transmittance is measurable at LP loading > 10%.

Amorphous Kraft lignin powder was used as received to produce membranes, in order to gain insights on the importance of the particle morphology for their cohesion. The lignin powder contains particle of large and polydisperse size, usually in the order of hundreds of microns [29,62]. They show lower specific surface compared to micro and nanosized round particles generated by the aerosol-flow method, and therefore they are less effective for the formation of membranes with CNF. **Figure 5b** shows an image of membranes produced using same amounts of kraft lignin (left), and aerosol-flow particles (right), in combination with given amounts of CNF. The top images show the aspect of the membranes under standard observation, while the bottom ones show the membranes using a box with backlight. As it can be observed, the light reveals defects in the membrane made using the amorphous kraft lignin, whereas the membrane containing aerosol-produced LP is homogeneous and completely opaque. Moreover, the mechanical properties of the membranes produced with amorphous kraft lignin are significantly reduced compared to those from LP, which are much easier to handle, **Figure 1c**. In this regard, the kraft lignin membranes are brittle, and break upon folding. Interestingly, the morphology of the particles plays a critical role on the way light interacts with the materials. Thus, the color of both membranes under normal viewing conditions is significantly different (**Figure 5b**): a clear-brown reflection is observed for the LPs membrane while dark brown is observed in the case of kraft lignin membranes.

An increasing CNF loading, up to 11%, produce membranes with a higher elasticity, as shown by DMA analysis (**Figure 5c**). However, CNF loading > 14% is detrimental as far as this property. These results reveal that the CNF loading selected previously for the LPs-CNF membranes (8%) is enough to produce self-standing materials, but their elasticity might be further improved, if required by the application. The decrease on the storage modulus for loadings > 14% CNF may be due to an increased interaction within the CNF when it is present in larger amounts. As depicted previously (**Figure 1c**), CNF tends to form a film, and this effect may be boosted when larger amounts are present. This may generate phase separation between CNF and LPs, diminishing their homogeneous interaction, and thus weakening the whole membrane structure.

The affinity towards water is another important parameter with regards to wetting ability and the performance of the membranes. This was assessed by monitoring the water contact angle, WCA. As indicated by the WCA in **Figure 5d**, the affinity towards water of the LP-based (LPs-CNF-WSA), pure CNF, and Whatman® 1 paper are significantly different. The absorption of the LP-based membrane and Whatman® 1 paper is faster compared to that of pure CNF membrane, as revealed by the dramatic

reduction of WCA during the initial absorption time. This result is interesting given the significantly different pore structure of these membranes.

Figure 5e shows a surface energy map for LP-based membranes (LPs-CNF-WSA), compared to that of CNF-membranes and Whatman® 1 paper. As shown, the values of the total surface free energy (SFE) of the LP-based membranes and that of Whatman® 1 paper are similar, and significantly higher than that of CNF. However, the major contribution to the total SFE of the LP-based membranes comes from its dispersive component, while that of Whatman® 1 paper and CNF-membranes comes from the polar contribution. The dispersive component in LP-based membranes is notably stronger than the polar one. This means that the membrane will show increased interaction (and thus, adhesion) to dispersive liquids and solids. This aspect may be interesting for the filtration of certain nonpolar liquids or to avoid the adsorption of polar particles. However, the membranes showed also good affinity with polar liquids, including water, as depicted previously in the WCA analyses.

Membrane fouling is the main cause of a declining permeant flux and loss of product quality in membrane filtration. Among the different sources of fouling, organic fouling is the most critical one. Moreover, a number of membrane technologies are aimed to separate proteins, as for example, in the cheese whey valorization and hemodialysis [61]. Thus, a low affinity of proteins to the membrane's materials may prevent protein fouling, and hence increased separation performance. Therefore, the adhesion of proteins to LP-based membranes was tested using lysozyme, as shown in **Figure 5f**. The results reveal that after several hours, the enzyme activity in the solution remained constant, which indicates that no enzyme was adsorbed on the surface of the membrane. These results are a first indication that despite the dispersive nature of the membranes, they may be useful in applications for protein fractionation.

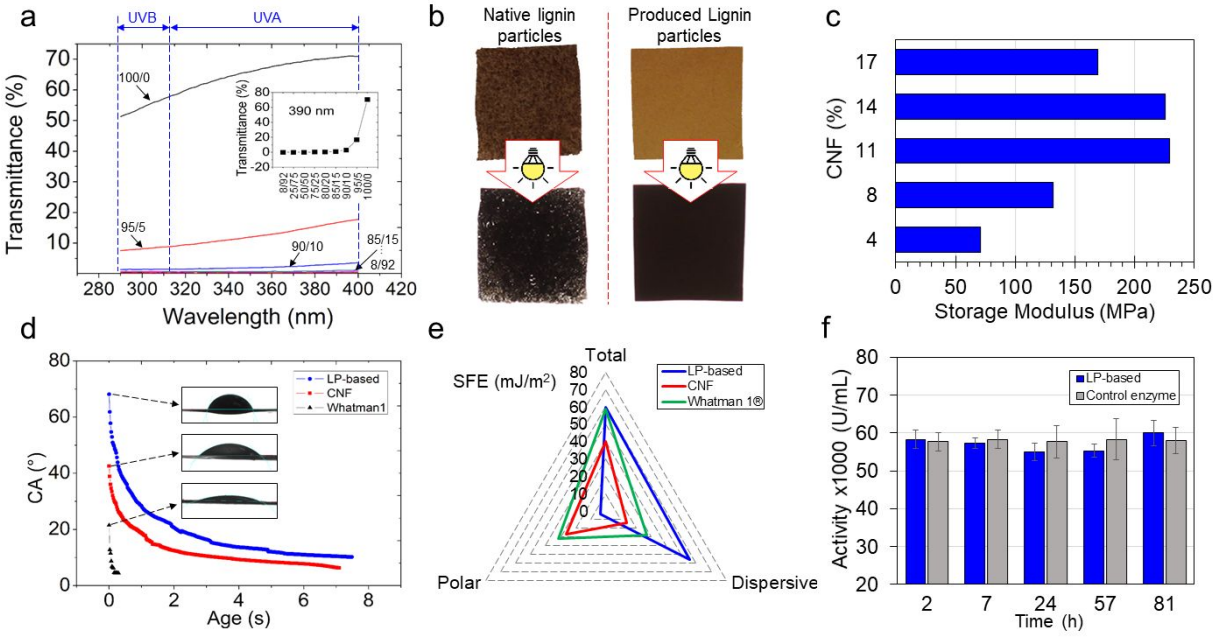

Figure 5. UV blocking capacity of membranes with varying CNF to LP ratios (CNF/LP), measured in the range 290-400 nm. The inset represents the evolution at a single

wavelength, 390 nm, as a function of the CNF-to-LP ratio (a). Comparison of the membranes produced using kraft lignin (membranes on the left) and LP (aerosol-flow particles, membrane on the right), observed under normal conditions (top) and using a light box with back illumination (bottom) (b). Storage modulus evolution of LP-based membranes with varying CNF loadings (c). Evolution of the contact angle vs. time upon water drop absorption on LP-based membranes, CNF membranes, and Whatman® 1 paper; the initial contact angles correspond to 68°, 42° and 22°, respectively (d). Surface free energy of LP-based membranes, CNF membranes, and Whatman® 1 paper (e). Protein (lysozyme) adsorption as indicated by the residual enzyme activity in the solution after filtration and illustrating the absence of fouling (f).

3.6. Further prospects: Patterning and 3D structuring

The combination of LPs and CNF produce membranes or layered materials by casting. However, the rheological properties of the casting suspension allow other shapes and structures. As a proof of concept, a 3D mold was built and filled with the LPs-CNF-WSA suspension (**Figure 6a**). After drying, the 3D object was de-molded while keeping the cohesion and being water-resistant. The LP-based suspension successfully filled the spaces inside the mold, being thus able to reproduce small features in the object. Also, the suspension was dispensed through a nozzle using an automatic syringe pump, allowing the deposition of 2D patterns on flat supports, **Figure 6b**. The pattern developed, as expected, was water-resistant after curing. The good processing ability of the suspension opens the door for 3D printing applications, to build almost all-lignin water-resistant objects with the introduction of WSA, as shown in **Figure 6**.

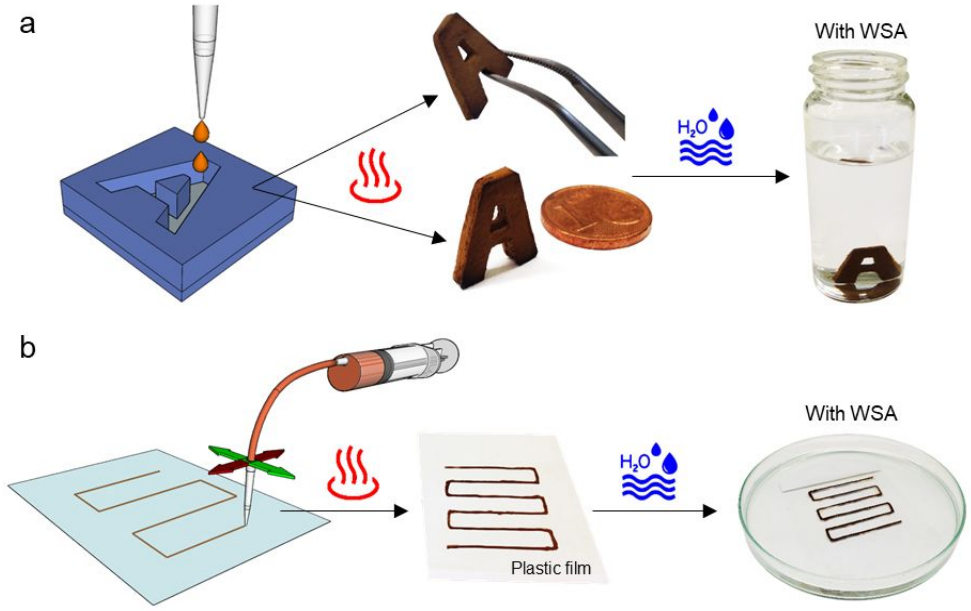

Figure 6. Development of 3D objects by mold-casting and with water resistance (a). 2D patterning as obtained by extrusion of the LP-based suspension over a flat surface (b).

4. Conclusions

We developed a new approach based on lignin particles (LPs) for the manufacture of materials of varying geometries. The structure, UV-blocking, water-absorption, and mechanical properties of these materials were studied by means of SEM imaging, UV-Vis transmittance, WCA, and DMA analyses. The structures comprised LPs held together with a minor component, cellulose nanofibers (CNF), applied at levels as small as 8 wt %, yet sufficient to confer integrity and flexibility through –OH interactions. For the first time, lignin is used as major structural component, reflecting its intrinsic properties. With the introduction of a wet-strength agent (WSA), membranes were developed, displaying water resistant and homogeneous sub-micron pore size distribution and water permeability –within a range of values needed in cross flow-filtration. Thus, active microfiltration membranes with antioxidant properties were demonstrated, effectively inhibiting oxidized radicals in effluent streams.

Supporting Information. Additional data such as an FTIR analysis of LPs, CNF, and a membrane containing 92% LPs and 8% CNF (Figure S1), rheological data of the aqueous suspensions of LP, CNF and LPs-CNF mixtures (Figure S2), a video showing the water resistance of the LPs-CNF membranes (with and without WSA), and a LPs leaching study from the membranes (Figures S3 and S4), are available in the Supporting Information.

Acknowledgements

Funding support is acknowledged from (1) FILMBIOCEL (No. CTQ2016-77936-R), (2) Fondo Europeo de Desarrollo Regional, FEDER, (3) MICROBIOCEL (No. CTQ2017-84966-C2-1-R), within the framework of the Spanish's MINECO and (3) the European Research Council (ERC) under the European Union's Horizon 2020 research and innovation programme (O.J.R. ERC Advanced Grant agreement No 788489, "BioElCell"). We are also grateful to the consolidated research group AGAUR 2014 SGR 534 at Universitat de Barcelona (UB). Special thanks are also due to the Serra Húnter Fellowship awarded to O.C. The authors would also like to thank Luiz Garcia Greca for synthesizing and providing the lignin particles used in this work.

References

(1) Guo, M.; Jin, T.; Nghiem, N. P.; Fan, X.; Qi, P. X.; Jang, C. H.; Shao, L.; Wu, C. Assessment of Antioxidant and Antimicrobial Properties of Lignin from Corn Stover Residue Pretreated with Low-Moisture Anhydrous Ammonia and Enzymatic Hydrolysis Process. *Appl. Biochem. Biotechnol.* **2018**, *184* (1), 350–365.

(2) Chen, S.; Lin, S.; Hu, Y.; Ma, M.; Shi, Y.; Liu, J.; Zhu, F.; Wang, X. A Lignin-Based

Flame Retardant for Improving Fire Behavior and Biodegradation Performance of Polybutylene Succinate. *Polym. Adv. Technol.* **2018**, *29* (12), 3142–3150.

(3) Dos Santos, P. S. B.; Erdocia, X.; Gatto, D. A.; Labidi, J. Bio-Oil from Base-Catalyzed Depolymerization of Organosolv Lignin as an Antifungal Agent for Wood. *Wood Sci. Technol.* **2016**, *50* (3), 599–615.

(4) Doblas, V. G.; Geldner, N.; Barberon, M. The Endodermis, a Tightly Controlled Barrier for Nutrients. *Curr. Opin. Plant Biol.* **2017**, *39*, 136–143.

(5) Figueiredo, P.; Lintinen, K.; Hirvonen, J. T.; Kostiainen, M. A.; Santos, H. A. Properties and Chemical Modifications of Lignin: Towards Lignin-Based Nanomaterials for Biomedical Applications. *Prog. Mater. Sci.* **2018**, *93*, 233–269.

(6) Gomes, E. D.; Rodrigues, A. E. Lignin Biorefinery: Separation of Vanillin, Vanillic Acid and Acetovanillone by Adsorption. *Sep. Purif. Technol.* **2019**, *216*, 92–101.

(7) Liang, S.; Wan, C. Biorefinery Lignin to Renewable Chemicals via Sequential Fractionation and Depolymerization. *Waste and Biomass Valorization* **2017**, *8* (2), 393–400.

(8) Ragauskas, A. J.; Beckham, G. T.; Biddy, M. J.; Chandra, R.; Chen, F.; Davis, M. F.; Davison, B. H.; Dixon, R. A.; Gilna, P.; Keller, M.; Langan, P.; Naskar, A.K.; Saddler, J.N.; Tschaplinski, T.J.; Tuskan, G.A.; Wyman, C.E. Lignin Valorization: Improving Lignin Processing in the Biorefinery. *Science.* **2014**, *344* (6185).

(9) Ponnusamy, V. K.; Nguyen, D. D.; Dharmaraja, J.; Shobana, S.; Banu, J. R.; Saratale, R. G.; Chang, S. W.; Kumar, G. A Review on Lignin Structure, Pretreatments, Fermentation Reactions and Biorefinery Potential. *Bioresour. Technol.* **2019**, *271*, 462–472.

(10) Chapter 5 - Lignin-Modified Thermoplastic Materials. In *Lignin Chemistry and Applications*; Huang, J., Fu, S., Gan, L., Eds.; Elsevier, 2019; pp 135–161.

(11) Norgren, M.; Edlund, H. Lignin: Recent Advances and Emerging Applications. *Curr. Opin. Colloid Interface Sci.* **2014**, *19* (5), 409–416.

(12) Laine, C.; Willberg-Keyriläinen, P.; Ropponen, J.; Liitiä, T. Lignin and Lignin Derivatives as Components in Biobased Hot Melt Adhesives. *J. Appl. Polym. Sci.* **2019**, *136* (38).

(13) Grossman, A.; Wilfred, V. Lignin-Based Polymers and Nanomaterials. *Curr. Opin. Biotechnol.* **2019**, *56*, 112–120.

(14) Shankar, S.; Reddy, J. P.; Rhim, J.-W. Effect of Lignin on Water Vapor Barrier, Mechanical, and Structural Properties of Agar/Lignin Composite Films. *Int. J. Biol. Macromol.* **2015**, *81*, 267–273.

(15) Zhang, Y.; Zhou, S.; Fang, X.; Zhou, X.; Wang, J.; Bai, F.; Peng, S. Renewable and Flexible UV-Blocking Film from Poly(Butylene Succinate) and Lignin. *Eur. Polym. J.* **2019**, *116*, 265–274.

(16) Zadeh, E. M.; O'Keefe, S. F.; Kim, Y.-T. Utilization of Lignin in Biopolymeric Packaging Films. *ACS Omega* **2018**, *3* (7), 7388–7398.

(17) Parit, M.; Saha, P.; Davis, V. A.; Jiang, Z. Transparent and Homogenous Cellulose Nanocrystal/Lignin UV-Protection Films. *ACS Omega* **2018**, *3* (9), 10679–10691.

(18) Sadeghifar, H.; Venditti, R.; Jur, J.; Gorga, R. E.; Pawlak, J. J. Cellulose-Lignin Biodegradable and Flexible UV Protection Film. *ACS Sustain. Chem. Eng.* **2017**, *5* (1), 625–631.

(19) Chapter 2 - Structure and Characteristics of Lignin. In *Lignin Chemistry and Applications*; Huang, J., Fu, S., Gan, L., Eds.; Elsevier, 2019; pp 25–50.

(20) Cusola, O.; Kivistö, S.; Vierros, S.; Batys, P.; Ago, M.; Tardy, B. L.; Greca, L. G.; Roncero, M. B.; Sammalkorpi, M.; Rojas, O. J. Particulate Coatings via Evaporation-Induced Self-Assembly of Polydisperse Colloidal Lignin on Solid Interfaces. *Langmuir* **2018**, *34*, 5759−5771.

(21) Rahikainen, J. L.; Martin-Sampedro, R.; Heikkinen, H.; Rovio, S.; Marjamaa, K.; Tamminen, T.; Rojas, O. J.; Kruus, K. Inhibitory Effect of Lignin during Cellulose Bioconversion: The Effect of Lignin Chemistry on Non-Productive Enzyme Adsorption. *Bioresour. Technol.* **2013**, *133*, 270–278.

(22) Salas, C.; Rojas, O. J.; Lucia, L. A.; Hubbe, M. A.; Genzer, J. Adsorption of Glycinin and β-Conglycinin on Silica and Cellulose: Surface Interactions as a Function of Denaturation, PH, and Electrolytes. *Biomacromolecules* **2012**, *13* (2), 387–396.

(23) Strasser, S.; Niegelhell, K.; Kaschowitz, M.; Markus, S.; Kargl, R.; Stana-Kleinschek, K.; Slugovc, C.; Mohan, T.; Spirk, S. Exploring Nonspecific Protein Adsorption on Lignocellulosic Amphiphilic Bicomponent Films. *Biomacromolecules* **2016**, *17* (3), 1083–1092.

(24) Pereira, A.; Hoeger, I. C.; Ferrer, A.; Rencoret, J.; Del Rio, J. C.; Kruus, K.; Rahikainen, J.; Kellock, M.; Gutiérrez, A.; Rojas, O. J. Lignin Films from Spruce, Eucalyptus, and Wheat Straw Studied with Electroacoustic and Optical Sensors: Effect of Composition and Electrostatic Screening on Enzyme Binding. *Biomacromolecules* **2017**, *18* (4), 1322–1332.

(25) Nguyen, N. A.; Bowland, C. C.; Naskar, A. K. A General Method to Improve 3D-Printability and Inter-Layer Adhesion in Lignin-Based Composites. *Appl. Mater. Today* **2018**, *12*, 138–152.

(26) Akato, K.; Tran, C. D.; Chen, J.; Naskar, A. K. Poly(Ethylene Oxide)-Assisted Macromolecular Self-Assembly of Lignin in ABS Matrix for Sustainable Composite Applications. *ACS Sustain. Chem. Eng.* **2015**, *3* (12), 3070–3076.

(27) Mainka, H. Lignin Powder as a Filler for Thermoplastic Automotive Lightweight Components. In *Annual Technical Conference - ANTEC, Conference Proceedings*; 2015; pp 245–248.

(28) Gkartzou, E.; Koumoulos, E. P.; Charitidis, C. A. Production and 3D Printing Processing of Bio-Based Thermoplastic Filament. *Manuf. Rev.* **2017**, *4*.

(29) Mimini, V.; Sykacek, E.; Hashim, S. N. A.; Holzweber, J.; Hettegger, H.; Fackler, K.; Potthast, A.; Mundigler, N.; Rosenau, T. Compatibility of Kraft Lignin, Organosolv Lignin and Lignosulfonate With PLA in 3D Printing. *J. Wood Chem. Technol.* **2019**,

39 (1), 14–30.

(30) Li, B.; Yuan, Z.; Schmidt, J.; Xu, C. C. New Foaming Formulations for Production of Bio-Phenol Formaldehyde Foams Using Raw Kraft Lignin. *Eur. Polym. J.* **2019**, *111*, 1–10.

(31) Zhang, J.; Fleury, E.; Brook, M. A. Foamed Lignin-Silicone Bio-Composites by Extrusion and Then Compression Molding. *Green Chem.* **2015**, *17* (9), 4647–4656.

(32) Mimini, V.; Kabrelian, V.; Fackler, K.; Hettegger, H.; Potthast, A.; Rosenau, T. Lignin-Based Foams as Insulation Materials: A Review. *Holzforschung* **2019**, *73* (1), 117–130.

(33) Miao, C.; Hamad, W. Y. Controlling Lignin Particle Size for Polymer Blend Applications. *J. Appl. Polym. Sci.* **2017**, *134* (14).

(34) Tian, D.; Hu, J.; Bao, J.; Chandra, R. P.; Saddler, J. N.; Lu, C. Lignin Valorization: Lignin Nanoparticles as High-Value Bio-Additive for Multifunctional Nanocomposites. *Biotechnol. Biofuels* **2017**, *10* (1).

(35) He, X.; Luzi, F.; Hao, X.; Yang, W.; Torre, L.; Xiao, Z.; Xie, Y.; Puglia, D. Thermal, Antioxidant and Swelling Behaviour of Transparent Polyvinyl (Alcohol) Films in Presence of Hydrophobic Citric Acid-Modified Lignin Nanoparticles. *Int. J. Biol. Macromol.* **2019**, *127*, 665–676.

(36) Farooq, M.; Zou, T.; Riviere, G.; Sipponen, M. H.; Österberg, M. Strong, Ductile, and Waterproof Cellulose Nanofibril Composite Films with Colloidal Lignin Particles. *Biomacromolecules* **2019**, *20* (2), 693–704.

(37) Yang, N.; Jia, X.; Wang, D.; Wei, C.; He, Y.; Chen, L.; Zhao, Y. Silibinin as a Natural Antioxidant for Modifying Polysulfone Membranes to Suppress Hemodialysis-Induced Oxidative Stress. *J. Memb. Sci.* **2019**, 86–99.

(38) Shin, S.-H.; Kodir, A.; Shin, D.; Park, S.-H.; Bae, B. Perfluorinated Composite Membranes with Organic Antioxidants for Chemically Durable Fuel Cells. *Electrochim. Acta* **2019**, *298*, 901–909.

(39) Rajesh, S.; Murthy, Z. V. P. Synthesis, Characterization and Application of Antioxidants Nanoparticles Incorporated Polymeric Membranes. *Sep. Sci. Technol.* **2019**, *54* (2), 247–257.

(40) Esmaeili, M.; Anugwom, I.; Mänttäri, M.; Kallioinen, M. Utilization of DES-Lignin as a Bio-Based Hydrophilicity Promoter in the Fabrication of Antioxidant Polyethersulfone Membranes. *Membranes (Basel).* **2018**, *8* (3).

(41) Ago, M.; Huan, S.; Borghei, M.; Raula, J.; Kauppinen, E. I.; Rojas, O. J. High-Throughput Synthesis of Lignin Particles (∼30 Nm to ∼2 Mm) via Aerosol Flow Reactor: Size Fractionation and Utilization in Pickering Emulsions. *ACS Appl. Mater. Interfaces* **2016**, *8* (35), 23302–23310.

(42) Serpen, A.; Capuano, E.; Fogliano, V.; Gökmen, V. A New Procedure to Measure the Antioxidant Activity of Insoluble Food Components. *J. Agric. Food Chem.*

2007, *55* (19), 7676–7681.

(43) Valls, C.; Roncero, M. B. Antioxidant Property of TCF Pulp with a High Hexenuronic Acid (HexA) Content. *Holzforschung* **2013**, *67* (3), 257–263.

(44) Cusola, O.; Valls, C.; Vidal, T.; Roncero, M. B. Conferring Antioxidant Capacity to Cellulose Based Materials by Using Enzymatically-Modified Products. *Cellulose* **2015**, *22* (4), 2375–2390.

(45) Guo, J.; Tardy, B. L.; Christofferson, A. J.; Dai, Y.; Richardson, J. J.; Zhu, W.; Hu, M.; Ju, Y.; Cui, J.; Dagastine, R. R.; Yarovsky, I.; Caruso, F. Modular Assembly of Superstructures from Polyphenol-Functionalized Building Blocks. *Nat. Nanotechnol.* **2016**, *11* (12), 1105–1111.

(46) Ejima, H.; Richardson, J. J.; Liang, K.; Best, J. P.; Van Koeverden, M. P.; Such, G. K.; Cui, J.; Caruso, F. One-Step Assembly of Coordination Complexes for Versatile Film and Particle Engineering. *Science (80-.).* **2013**, *341* (6142), 154–157.

(47) Maina, J. W.; Cui, J.; Björnmalm, M.; Wise, A. K.; Shepherd, R. K.; Caruso, F. Mold-Templated Inorganic-Organic Hybrid Supraparticles for Codelivery of Drugs. *Biomacromolecules* **2014**, *15* (11), 4146–4151.

(48) Gause, K. T.; Yan, Y.; Cui, J.; Obrien-Simpson, N. M.; Lenzo, J. C.; Reynolds, E. C.; Caruso, F. Physicochemical and Immunological Assessment of Engineered Pure Protein Particles with Different Redox States. *ACS Nano* **2015**, *9* (3), 2433–2444.

(49) Mattos, B. D.; Greca, L. G.; Tardy, B. L.; Magalhães, W. L. E.; Rojas, O. J. Green Formation of Robust Supraparticles for Cargo Protection and Hazards Control in Natural Environments. *Small* **2018**, *14* (29).

(50) Sun, X.; Mei, C.; French, A. D.; Lee, S.; Wang, Y.; Wu, Q. Surface Wetting Behavior of Nanocellulose-Based Composite Films. *Cellulose* **2018**, *25* (9), 5071–5087.

(51) Zhang, H.; Wang, X.; Liang, Y. Preparation and Characterization of a Lithium-Ion Battery Separator from Cellulose Nanofibers. *Heliyon* **2015**, *1* (2).

(52) Sehaqui, H.; Zimmermann, T.; Tingaut, P. Hydrophobic Cellulose Nanopaper through a Mild Esterification Procedure. *Cellulose* **2014**, *21* (1), 367–382.

(53) Varanasi, S.; Garusinghe, U.; Simon, G. P.; Garnier, G.; Batchelor, W. Novel In-Situ Precipitation Process to Engineer Low Permeability Porous Composite. *Sci. Rep.* **2018**, *8* (1).

(54) Aaltosalmi, U.; Kataja, M.; Koponen, A.; Timonen, J.; Goel, A.; Lee, G.; Ramaswamy, S. Numerical Analysis of Fluid Flow through Fibrous Porous Materials. *J. Pulp Pap. Sci.* **2004**, *30* (9), 251–255.

(55) Gigac, J.; Stankovská, M.; Fišerová, M. Comparison of Capillary Flow Porometry and Mercury Intrusion Porosimetry in Determination Pore Size Distribution of Papers. *Wood Res.* **2017**, *62* (4), 587–596.

(56) Kalliopi K., A. *Pore Structure of Cement-Based Materials: Testing, Interpretation and Requirements*, 1st Edition.; Bentur, A., Mindess, S., Eds.; CRC press: London ,

2005.

(57) Sobieski, W. The Use of Path Tracking Method for Determining the Tortuosity Field in a Porous Bed. *Granul. Matter* **2016**, *18* (3).

(58) Ghassemi, A.; Pak, A. Pore Scale Study of Permeability and Tortuosity for Flow through Particulate Media Using Lattice Boltzmann Method. *Int. J. Numer. Anal. Methods Geomech.* **2011**, *35* (8), 886–901.

(59) Barrande, M.; Bouchet, R.; Denoyel, R. Tortuosity of Porous Particles. *Anal. Chem.* **2007**, *79* (23), 9115–9121.

(60) Jena, A.; Gupta, K. *Advanced Technology for Evaluation of Pore Structure Characteristics of Filtration Media to Optimize Their Design and Performance*; Ithaca, NY, 2002.

(61) Baker, R. W. *Membrane Technology and Applications*, Second Edition.; John Wiley & Sons, Ltd.: Menlo Park, California, 2004.

(62) Gkartzou, E.; Koumoulos, E. P.; Charitidis, C. A. Production and 3D Printing Processing of Bio-Based Thermoplastic Filament. *Manuf. Rev.* **2017**, *4*.

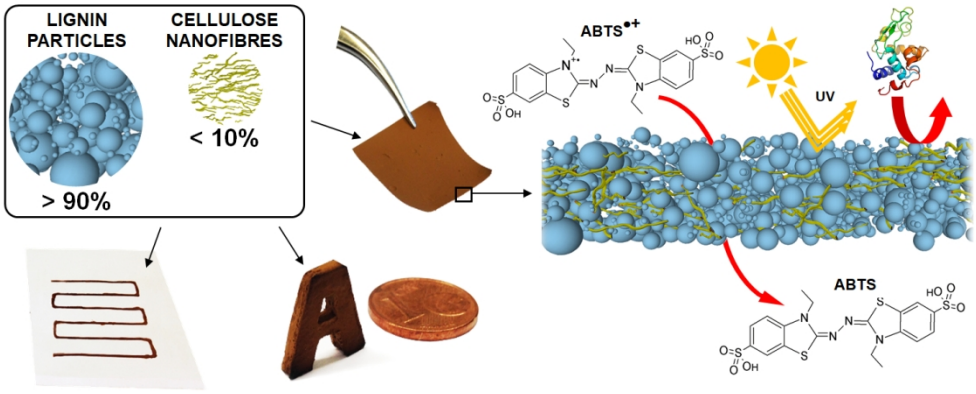

Graphical Abstract

129x51mm (300 x 300 DPI)

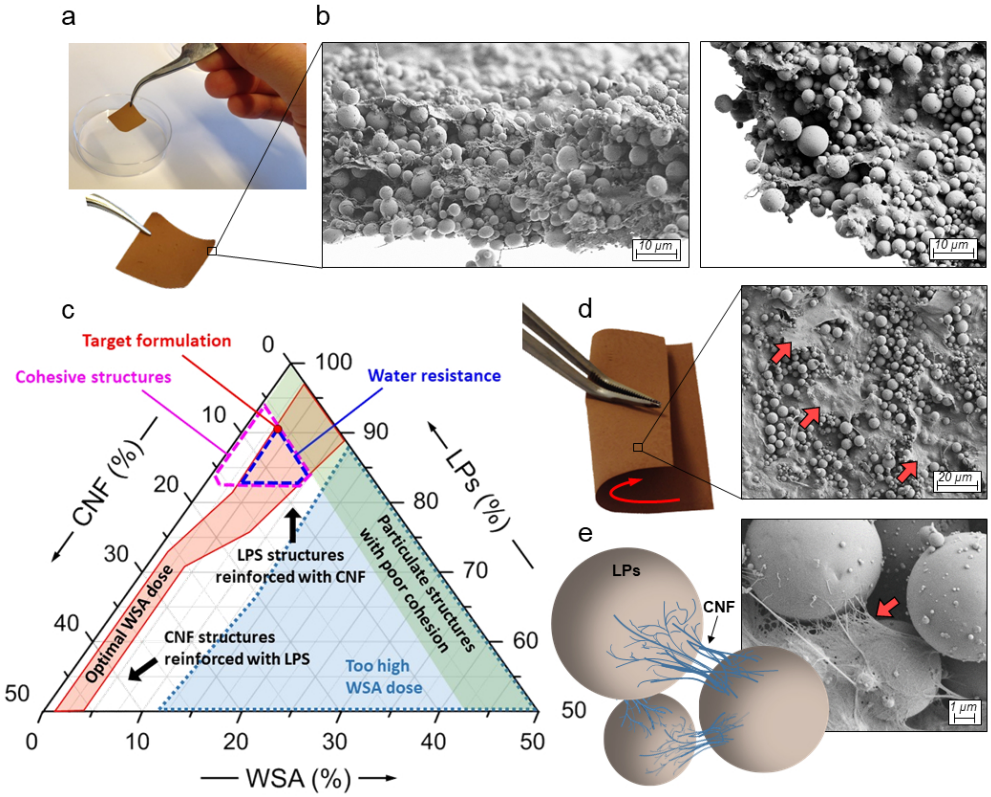

Figure 1. Self-standing LPs-CNF membranes (shown in (a) is the case of systems with 8% wt CNF). SEM cross-sections of the membrane in (a) are shown in (b). Ternary phase diagram indicating the composition (LP, CNF, WSA) that leads to membranes with good cohesion and water-strength, including the optimal conditions for maximizing LP loading while allowing for water resistance (c). The flexibility and folding ability of LP-based membranes is illustrated with a photo in (d), along with a SEM image of the surface morphology where CNF formed continuous film regions (d, red arrows). Schematic diagram and SEM image showing the role of the CNF bridging the particles together within the particulate structure (e).

277x221mm (96 x 96 DPI)

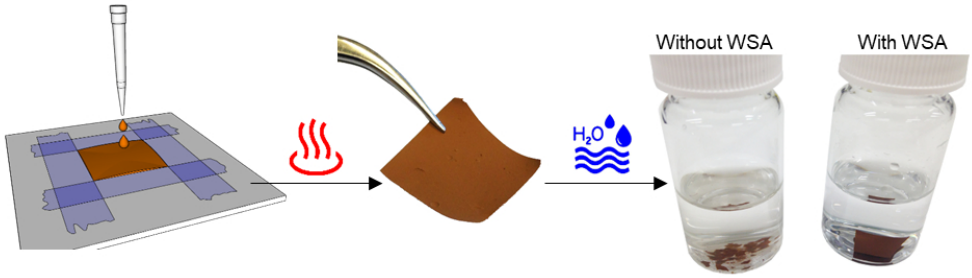

Figure 2. Membrane casting on a flat support, photo of the obtained membrane, and illustration of a test for water resistance after treatment with WSA.

254x72mm (96 x 96 DPI)

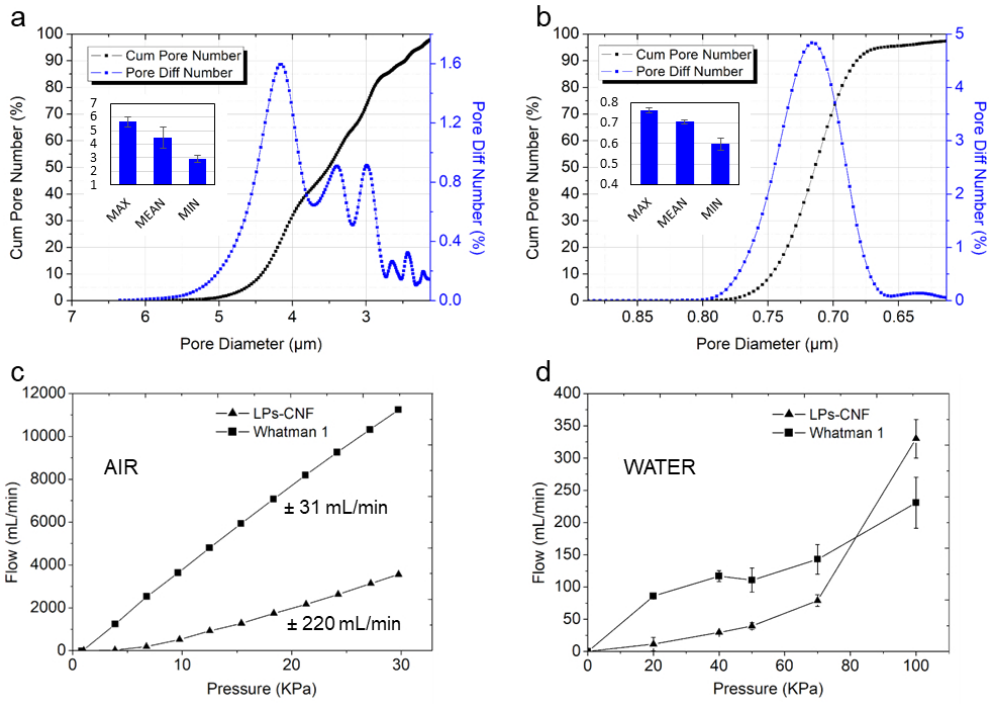

261x188mm (96 x 96 DPI)

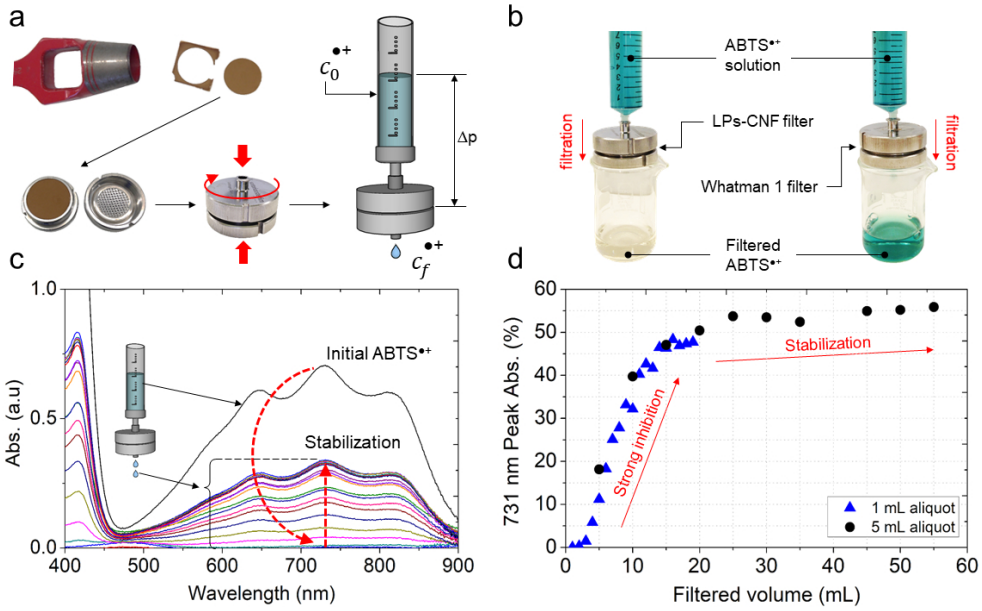

Figure 4. Assembly of LP-based membranes and mounting on a Sartorius™ Stedim stainless-steel Syringe Filter Holder for constant pressure filtration of a cationic radical (a). Filtration of ABTS•+radical solution using Whatman□ 1 filter paper (right) and LP-based membranes (left); the remarkable decolorization of the blueish ABTS•+ radical after passage through the LP-based membrane is clearly seen (b). UV-Vis spectra of the initial ABTS•+ radical and evolution after passage through the LP-based membrane; a clear decrease and further stabilization is depicted (c). Evolution of the ABTS•+ radical 731 nm peak after filtration through the ABTS•+ radical (as % of the initial absorbance) taken after filtration of 1 mL aliquots (▲) and 5 mL aliquots (●) (d).

307x188mm (96 x 96 DPI)

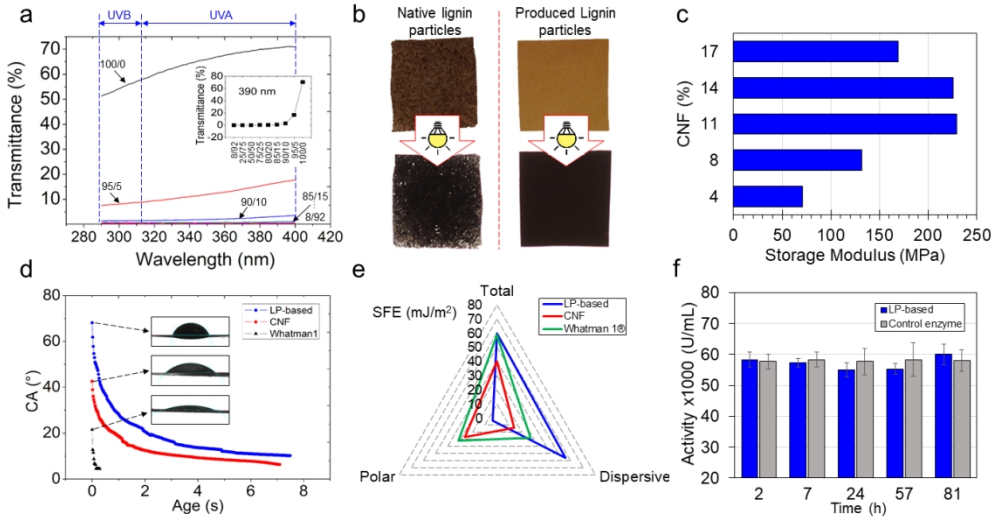

369x192mm (96 x 96 DPI)

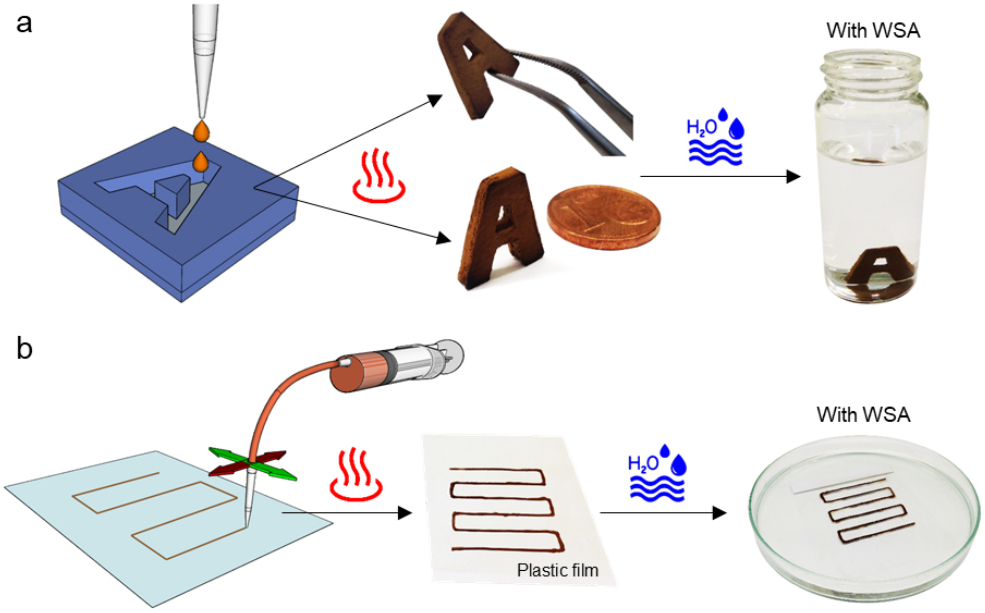

Figure 6. Development of 3D objects by mold-casting and with water resistance (a). 2D patterning as obtained by extrusion of the LPs-CNF over a flat surface (b).

242x152mm (96 x 96 DPI)